

The emerging role of 4D synchrotron X-ray micro-tomography for climate and fossil energy studies: five experiments showing the present capabilities at beamline 8.3.2 at the Advanced Light Source

Marco Voltolini,^{a*} Abdelmoula Haboub,^{b,†} Shan Dou,^a Tae-Hyuk Kwon,^c Alastair A. MacDowell,^b Dilworth Y. Parkinson^b and Jonathan Ajo-Franklin^a

^aEarth and Environmental Sciences Area, Lawrence Berkeley National Laboratory, 1 Cyclotron Road, Berkeley, CA 94720, USA, ^bAdvanced Light Source, Lawrence Berkeley National Laboratory, 1 Cyclotron Road, Berkeley, CA 94720, USA, and ^cKorea Advanced Institute of Science and Technology, 373-1 Guseong-dong, Yuseong-gu, Daejeon, South Korea

*Correspondence e-mail: mvoltolini@lbl.gov

Edited by P. A. Pianetta, SLAC National Accelerator Laboratory, USA (Received 26 April 2017; accepted 29 August 2017; online 13 October 2017)

Continuous improvements at X-ray imaging beamlines at synchrotron light sources have made dynamic synchrotron X-ray micro-computed tomography (SXR- μ CT) experiments more routinely available to users, with a rapid increase in demand given its tremendous potential in very diverse areas. In this work a survey of five different four-dimensional SXR- μ CT experiments is presented, examining five different parameters linked to the evolution of the investigated system, and tackling problems in different areas in earth sciences. SXR- μ CT is used to monitor the microstructural evolution of the investigated sample with the following variables: (i) high temperature, observing *in situ* oil shale pyrolysis; (ii) low temperature, replicating the generation of permafrost; (iii) high pressure, to study the invasion of supercritical CO₂ in deep aquifers; (iv) uniaxial stress, to monitor the closure of a fracture filled with proppant, in shale; (v) reactive flow, to observe the evolution of the hydraulic properties in a porous rock subject to dissolution. For each of these examples, it is shown how dynamic SXR- μ CT was able to provide new answers to questions related to climate and energy studies, highlighting the significant opportunities opened recently by the technique.













Keywords: X-ray microCT; *in situ* imaging; earth and energy sciences.

[Similar articles](#)[PowerPoint slides](#)


1. Introduction

In the field of earth sciences, X-ray microtomography has already proven to be an extremely useful technique due to its ability to non-destructively characterize the microstructure of a sample in three dimensions. X-ray microtomographic experiments can be carried out using either conventional laboratory-based sources (X-ray tubes) or synchrotron X-rays, and, following the developments in the field, geoscientists have utilized this technique to study a growing range of topics [see, for example, Gualda *et al.* (2010) and Cnudde & Boone (2013) for reviews]. With X-ray microtomography, the use of synchrotron radiation presents some advantages when compared with conventional X-ray tube sources; these advantages generally include monochromaticity (avoiding beam hardening artifacts), high spatial coherence (allowing better phase-contrast imaging), and high X-ray flux at the sample (allowing faster measurements). For these reasons synchrotron X-ray micro-computed tomography (SXR- μ CT) has become a technique of choice for many geoscience applications. One of the first topics related to geoscience to take full advantage of the capabilities of synchrotron SXR- μ CT was fossil energy research, with specific emphasis on the reservoir rock characterization at the pore scale. Early advances were assisted by such industry investments; Exxon funded and operated, until its decommissioning, its own SXR- μ CT beamline (X2B) at the Brookhaven National Laboratory [see Dunsmuir *et al.* (2006) for fossil-fuel-related examples], started to publish data in 1999, and published its first reservoir rock characterization article the following year (Zhou *et al.*, 2000). At present, all of the current synchrotron light sources capable of hard X-ray imaging are using SXR- μ CT for earth-sciences-related research. The most prominent example is the GSECARS group at the Advanced Photon Source, which has also pioneered the use of environmental cells for *in situ* imaging (Rivers *et al.*, 1999; Rivers & Wang, 2006; Yu *et al.*, 2016), with an emphasis on extreme temperature (T) and pressure (P) measurements using the Paris-Edinburgh type of cell (see also: Bromiley *et al.*, 2009), similar in concept to those used for neutron and X-ray diffraction experiments (Besson *et al.*, 1992; Le Godec *et al.*, 2005). Other SXR- μ CT synchrotron beamlines currently work on a regular basis with geoscientist users and developing their own *in situ* devices (e.g. Renard *et al.*, 2016); a partial list is given by Fuisseis *et al.* (2014a).

Indeed, one of the main advantages of modern SXR- μ CT facilities is the use of hard X-rays and their ability to penetrate and take advantage of environmental cells aimed at studying samples under non-ambient conditions. The requirement of both high-energy X-rays and a high photon flux is of paramount importance: environmental cells are usually highly attenuating, and dynamic systems need to be measured rapidly to avoid issues such as motion artefacts. For this reason nowadays pink or (filtered) white beams are usually preferred to monochromatic beams. Studies aimed at imaging rock samples at the elevated pressures and temperatures encountered in subsurface reservoirs (e.g. oil reservoirs, CO₂ geological storage, etc.) have only been conducted during the last

few years, with the development of environmental fluid cells specifically designed for SXR- μ CT experiments (Andrew *et al.*, 2013 ; Iglaier *et al.*, 2013 ; Füsseis *et al.*, 2014b ). With the last generation of upgrades at synchrotron X-ray imaging beamlines, a step further has been more frequently targeted: the study of the dynamics of geological systems, thus adding a fourth dimension to the data (e.g. Armstrong *et al.*, 2014 ; Kerkar *et al.*, 2014 ; Andrew *et al.*, 2013 ), with the last trend being ultrafast SXR- μ CT, implemented by taking advantage of the high brilliance of specific beamlines such as ID15 at the ESRF (Di Michiel *et al.*, 2005 ), often combined with the latest generation of CMOS detectors with local RAM storage to address the bottleneck of data transfer speed (e.g. Berg *et al.*, 2013 ; Youssef *et al.*, 2014 ). Four-dimensional (4D) SXR- μ CT is a rapidly developing field in general, and first publications showing the time evolution of materials are starting to be found in the literature [see, for example, Baker *et al.* (2012 ), Landry *et al.* (2014 ), and Panahi *et al.* (2014 )] for experiments related to earth sciences].

These newly developed experimental capabilities are evidently opening new and important opportunities to study a wide range of dynamic systems. The geoscience community is starting to benefit from this with an ongoing effort to build novel environmental cells fulfilling the specific requirements in terms of temperature, flow, chemistry, pressure, *etc.* allowing the field to tackle scientific questions on the broadest range of topics. In this context, we are presenting a survey of examples describing how *in situ* 4D SXR- μ CT is currently being developed by a joint effort of the 8.3.2 beamline of the Advanced Light Source and the Earth and Environmental Sciences Area of the Lawrence Berkeley National Laboratory to help find answers in a diverse range of earth science fields.

In the context of *in situ* dynamic experiments aimed at imaging dynamic systems, this work illustrates a series of different dynamic SXR- μ CT experiments related to climate and fossil energy studies, all performed at beamline 8.3.2 of the Advanced Light Source at Lawrence Berkeley National Laboratory, USA (MacDowell *et al.*, 2012 ). All the work has been carried out by the authors and represents state-of-the-art examples for that facility concerning dynamic X-ray imaging in the field of earth sciences. For each of the five experiments presented, targeting diverse geosciences-related topics, we will observe the effect over time of five different parameters of the examined dynamic systems. (i) *High temperature*, the pyrolysis of an oil shale sample aimed at observing the evolution of the porosity and the potential impact for oil extraction. (ii) *Low temperature*, the evolution of the microstructure in permafrost during freezing: are the current freezing models correct? (iii) *High pressure*, how does the displacement of brine by drainage of scCO₂ proceed? Can it be predicted? (iv) *Uniaxial stress*, which are the basic mechanisms involved in

the closure of fractures filled with proppant in shales? (v) *Reactive transport*, how does the chemical dissolution of a rock affect its hydraulic properties?

The aim of this article is to highlight the current flexibility and the wide range of information 4D SXR- μ CT can provide to geoscientists, rather than to explain the experiments in detail. It has been addressed by showing five very diverse examples, tackling specific earth-sciences-related problems, all performed by the authors at a single synchrotron imaging beamline. For each example presented, we will first briefly explain the context of the problem investigated, then we will describe the SXR- μ CT experimental approach and the results, and finally we will summarize the unique kind of information obtained from the specific experiment, coupled with some sample-specific data analysis, showing the unique kind of information obtained. This provides a both complete and concise summary of some of the many new possibilities opened by this technique and its potential impact in the close future.

2. 4D SXR- μ CT experiments and results

2.1.) High temperature: pyrolysis of oil shale

Oil shales are an unconventional fossil fuel resource with high potential importance, but because hydrocarbons are tightly trapped their extraction is often difficult and often not economically viable. One of the extraction methods proposed is *in situ* subsurface pyrolysis, which converts kerogen to liquid or gas phases and thermomechanically fractures the shale (Tiwari *et al.*, 2013; Panahi *et al.*, 2014) so they can be more easily extracted. While bulk experiments have been carried out for decades, the process at the micrometer scale is still poorly understood, and a better knowledge of the different mechanisms involved in the generation and migration of the hydrocarbon could lead to better extraction procedures.

The environmental cell for the sample used for this experiment is shown in Fig. 1(a) [described in detail by Bale *et al.* (2013)], where a visual summary of the cells used for the experiments presented in this work is shown. The sample is mounted onto a vertical loading stage (capable of uniaxial compression or extension) and surrounded by six halogen lamps used as heating sources. A Green River oil shale (Utah) sample (~6 mm cylinder, with the lamination planes roughly vertical) is held in place with just enough stress to confine it vertically. After taking a baseline image at room temperature, the temperature was increased to 400°C and the evolution of the sample was kept at constant temperature for 6 h, taking measurements every 2 h to monitor the temporal variation of the sample at constant temperature. The data were collected using 28 keV monochromatic X-rays via a double multilayer monochromator, with an exposure time of 450 ms for each of the 2049 projections. Pixel size was 3.26 μ m and the sample-to-detector distance was ~11 cm.

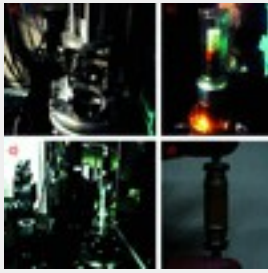





Figure 1

Visual summary of the environmental cells used in this article. (a) The cell used for high-temperature and uniaxial compression (halogen lamps unmounted, to show the sample position). (b) Detail of the cooling cell, with the copper cold finger below the PTFE tube containing the sample. (c) The high-pressure cell mounted on the rotating stage at the beamline, prior to mounting all the tubing system. (d) Detail of the sample, jacketed with a heat-shrink tube, used for the flow experiment at low pressure.

We present a visualization of the results in Fig. 2(a) , with volume renderings virtually cut to show the interior of the sample at each time point. The images show that the majority of the changes occur between the first two images, *i.e.* in the first 2 h, with much more subtle changes taking place afterwards. The most significant change in structure that can be found from visual inspection is the swelling in some inclusions due to the kerogen phase change and the generation of planar micro-crack arrays. Digital slices through the image volumes (Fig. 2b ) make it clear that the fracturing is highly anisotropic: the boundary of the sample evolved from a perfect circle to an ellipse with the long axis perpendicular to the lamination plane. Another prominently visible change shown in Fig. 2(a)  is the generation of an 'S' fold with the flex line roughly at the center of the sample. This can be explained by the vertical confinement of the sample: the sample expands both parallel to and perpendicular to the sample, though the parallel expansion is much larger; nevertheless, the extent of expansion along the laminations plane is still significant, especially considering the length of the sample, therefore a microfold was generated to accommodate this expansion.

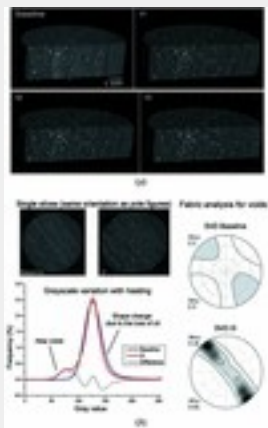





Figure 2

(a) Heating sequence of the Green River oil shale sample. Volume rendering with vertical cut. (b) Reconstructed slices from the baseline and the last dataset after heating (t3) to show the expansion of the sample and the development of the new voids. Gray-level histograms (normalized) of the unheated and heated sample to show the variation of the patterns due to the loss of oil + water. On the right, SVD pole figures showing the evolution of the anisotropy of the voids are plotted.

A quantification of the evolution of the fracture anisotropy is important, since fracture anisotropy is linked to both hydrological changes [permeability, *e.g.* Sutton *et al.* (2004 )]) as well as mechanical properties such as seismic wave velocities (Votolini *et al.*, 2008 )], the latter of which affect the interpretation of seismic surveys in the field (*e.g.* reservoir monitoring). To quantify this property, we performed a star volume density (SVD) analysis (Ketcham, 2005 ) and plotted the

pole figures (PFs) derived from the orientation density function obtained from the SVD data (Voltolini *et al.*, 2011) relative to the anisotropy of the porosity. The top SVD PF in Fig. 2(b) (right panel) shows that the few voids that are resolved in the untreated sample are slightly anisotropic and roughly parallel to the lamination plane. After pyrolysis [6 h, sample 't3', bottom right panel in Fig. 2(b)] the SVD plot shows that the anisotropy is enhanced because of the development of the newly formed lens-shaped voids (fractures), again parallel to the lamination. This evolution should have a significant impact in the mechanical and flow properties of the material with subsequent effect on understanding the hydrocarbon extraction mechanisms.

The bottom left panel in Fig. 2(b) shows a histogram analysis, based on the X-ray attenuation, of these two datasets. The voxel values in the images correspond to X-ray attenuation coefficients of the sample, which are determined by a combination of the chemical composition in a given voxel and the physical density of the material in that voxel. Tracking changes in the histograms of the voxel values between images can give a quantitative measure of the sample changes, taking account of features below the resolution (partial volume effects). Since we can safely assume that the solid phase (quartz, calcite, feldspars, pyrite, clays, *etc.*) has constant X-ray attenuation properties, changes in voxel values would be proportional to the amount of hydrocarbons and water expelled. In practice, histogram analysis is complicated by problems including image artifacts and phase-contrast contributions, sub-resolution structures and changes in attenuation of the solid phase, for example due to collapse after water loss or crystal structure shrinkage (Bray *et al.*, 1998; Ferrage *et al.*, 2007), but semi-quantitative results can still be achieved. In Fig. 2(b) the histogram (calibrated to air attenuation) is shown for the same slice of the sample before and after pyrolysis, along with a plot of the difference between them. The main peak (corresponding to attenuation values of clay + quartz + feldspars) does not shift, but the peak becomes sharper and the asymmetry present on the right side in the sample before heating almost disappears. In the reacted sample a new peak at lower attenuation values is present. These changes can be related to the loss of water and hydrocarbon from the solid phase, and the creation of new voids, making this analysis a useful tool for tracking the evolution of the system despite the presence of sub-resolution features which are especially important in shales and clay-bearing materials.

While an average analysis, as provided by the global grayscale histogram, is useful, to be able to understand where in the sample this density loss has occurred provides important hints about the localization of recoverable hydrocarbons, highlighting features such as heterogeneities. A simple image subtraction does not work because of the different shape of the sample before and after the reaction, therefore a more complex procedure is needed. To be able to calculate the difference of the material before and after reaction, besides operating an image registration of two equivalent slices, we need to 'close' the voids generated by the pyrolysis. This 'shrinkage' has been

accomplished on the reconstructed slice using a combination of a digital image correlation (DIC) script, derived from Eberl *et al.* (2006), used to track the movement of the voxels sample, combined with *bUnwarpJ* (Arganda-Carreras *et al.*, 2008), used to shrink the sample in the original circular shape. A 5 pixel-radius median filter was applied (to both reacted and unreacted slices) to eliminate the noise due especially to the bright pyrite spots, which were not perfectly constant in the two slices. Given the approach used, the resolution of this analysis resulted in reduced resolution compared with the original images, and averaging over 25 voxel was needed. Nevertheless, a useful map shows, in a semi-quantitative fashion, where the volatile compounds that have been expelled can be obtained (see Fig. 3). The map obtained shows that there are in fact laminations (in red) where the largest difference is concentrated.

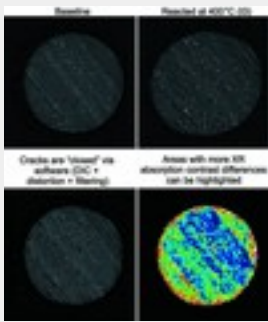


Figure 3

Slices showing the local analysis of density loss. At the top, the sample before and after pyrolysis (after 12 h) is shown (single slice). At the bottom, the slice after pyrolysis with the voids closed *via* software and a difference image showing where the loss in density happened are shown, highlighting the layers richer in mobilizable oil; red indicates a greatest density loss.

2.2. Low temperature: distribution of brine during permafrost generation by freezing

Permafrost degradation has a significant impact on greenhouse gas fluxes (Koven *et al.*, 2011), and the understanding of permafrost under climate change warming scenarios will likely have an impact on warming trajectories. Seismic techniques are a proposed monitoring tool, and permafrost microstructure has a large impact on the interpretation and modeling of seismic data, especially during the freezing stage, since ice distribution exerts a dominant control on the relationship between mechanical properties and ice content (e.g. Dou *et al.*, 2016, 2017). Applying standard models to freezing curves from experiments where measured ultrasonic p-wave velocities during freezing of a sand + brine (2.5 M NaCl) mixture in a cylindrical vessel highlights the inadequacy of these models, as shown in Fig. 4. This figure shows the data, along with plots of the expected results, for four standard models: (i) ice nucleation at grain contacts (leading to strong cementation of the system even during early stages of crystallization); (ii) uniform coating of grains, with ice depositing in layers (eventually cementing the system); (iii) ice patches form, similar to grains (leading to weaker cementation); (iv) ice nucleation in the center of the largest pores (expanding to cement some parts of the sample).

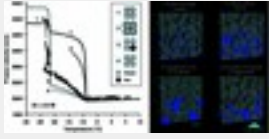


Figure 4

Ultrasonic p-wave velocities measurement in a freezing experiment of a sand + brine mixture. The calculated wave velocities using the four classic models for the system microstructure are also plotted to highlight the inadequacy of the models to describe the system. On the right, a simulation of the ice distribution (blue) in a real sand pack dataset with a freezing front from the bottom has been calculated to highlight the difference with the real data, presented in Fig. 5.

To better understand the real microstructure, we decided to pursue an *in situ* freezing experiment with SXR- μ CT to precisely monitor how ice develops in a loose sand pack immersed in brine. The experiment consisted of the generation of a ~ 3 mm permafrost sample *in situ* at the beamline. We used a low-temperature cell (Fig. 1b) consisting of a Peltier stage able to reach -14°C , with the freezing front propagating from the copper cold finger at the base of the sample. The sample is enclosed in a PTFE tube surrounded by a double-walled PVC cap acting as an insulator. Data were collected using 25 keV monochromatic X-rays, with an exposure time of 550 ms for each of the 1441 projections. Pixel size was $3.44\text{ }\mu\text{m}$ and the sample-to-detector distance was ~ 5 cm. A 1.5 M KI brine was used both as a contrast agent and to reach a realistic salinity level. Fig. 5(a) shows the sequence of images collected as the sample is frozen, progressively lowering the temperature (the freezing front advances from the bottom, where the end of the cold finger is located). The resulting microstructure is very complex, with acicular and lath-shaped ice crystals growing from the freezing front in a roughly vertical direction. In Fig. 5(b) a horizontal slice of the sample at -14°C shows in detail the extreme complexity of the microstructure generated by the freezing process, with the brine film between ice crystals, and on the surface of sand grains visually enhanced by the phase contrast effect. As can be seen in Fig. 5(b), anisotropic ice needles with brine-filled inter-crystal spaces form, aligned with the vertical temperature gradient. Salinity gradients are present, especially close to the freezing front, and the brine, as expected, becomes more and more concentrated in KI with the progression of ice crystallization (the X-ray attenuation of the fluid clearly increases). Residual brine is trapped at ice crystal interfaces and at the sides of the grains facing the freezing front, forming a brine layer on the lower portion of the sand grains, while ice crystals grow upwards from the side of the sand grain opposite to the freezing front. This leads to a sort of trailing effect, with the 'trails' of residual brine starting from the equator of the grains and widening upwards. The growth of the ice crystals pushes the grains (and the residual brine) upwards and increases the separation between the grains, decreasing the number of grain contacts, a fact that would dramatically impact seismic properties of the material under low stress conditions.

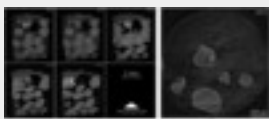


Figure 5

(a) Sequence of renderings (vertical cut) from the freezing experiment. It is possible to appreciate the growth of ice from the bottom of the sample (freezing front) and the residual brine trapped at the ice crystal

boundaries. The brine facing the freezing front also increases in salinity (increase in X-ray attenuation → higher gray value) while the freezing proceeds. (b) Reconstructed slice of the sample at -14°C , close to the bottom of the sample. It is possible to appreciate the complexity of the pattern of residual brine generated by the crystallization of the ice needles and platelets. A film of residual brine surrounding the lower part of the sand grains is also visible.

This experiment shows how the commonly used models are very far from what it is observable experimentally, and new and more complex models are needed in order to correctly calculate seismic wave velocities in a freezing sand pack. The experiments also highlight how, from observations at the micrometer scale, 4D SXR- μCT can yield important information required to understand processes with regional scale consequences.

2.3. High pressure: drainage of CO_2 at reservoir conditions

In the last decade, the scientific community has made a significant effort to investigate geological CO_2 sequestration (GCS) (e.g. Herzog, 2001 →; Metz *et al.*, 2005 →). SXR- μCT has proven extremely useful for related investigations at the pore scale (e.g. Silin *et al.*, 2011 →), but *in situ* experiments require cells that allow the observation of the sample at the proper P/T conditions of the targeted reservoir rocks. We developed the tri-axial cell shown in Fig. 1(c) →, which is able to reach reservoir-like pressures (with a limited range of controlled temperatures), up to ~ 3250 psi (~ 22.4 MPa), with a system of syringe pumps allowing the regulation of flow, pore pressure and confining pressure, required to study phenomena such as CO_2 invasion, imbibition, *etc.* and multiphase/reactive transport more in general.

Here we review an experiment presented in detail by Voltolini *et al.* (2017 →) in which we monitor the invasion of supercritical CO_2 (scCO_2) in a Domengine sandstone sample under realistic reservoir conditions: 50°C , 1550 psi (10.7 MPa) of confining pressure and 1225 psi (8.4 MPa) of pore pressure. Data were collected using filter-hardened white X-rays, with an exposure time of 80 ms for each of the 1441 projections and with a pixel size of $4.44\text{ }\mu\text{m}$. When using more attenuating systems, such as the one presented here, where the X-ray beam needs to go through the outer aluminium alloy shell, the water in the confining pressure annulus, and the jacket of the sample, before finally reaching the sample itself, the X-ray flux in monochromatic mode at the required energy is too low to obtain adequately short exposure for dynamic studies. In Fig. 6(a) → a sequence of two-dimensional projections showing the invasion (from the top) of the scCO_2 in the sandstone pore space is presented. For this experiment the main interest was mapping the distribution of scCO_2 to find its relationship with the microstructure of the host rock and to understand how the topology of the pore space influences the distribution of the scCO_2 . If a clear relationship was found, then a predictive model can be built. The measurement to modeling tool chain used to analyze the recovered volume is explained by Voltolini *et al.* (2017 →). The model was based on the calculated

local thickness value (Dougherty & Kunzelmann, 2007), coupled with a connected component labeling procedure (Hu *et al.*, 2005) that mimics the drainage of a perfectly non-wetting fluid, given the geometry of the inlet and proper boundary conditions. Fig. 6(b) shows the projection calculated based on our model, equivalent to the measured one: the similarity is evident. On the right side of Fig. 6(b) the volume rendering of a vertical slice from the measured dataset with the two different fluids highlighted is shown; below, the same volume with the calculated distribution (calculated from the 'dry' baseline dataset) is shown. The similarity of the measured and calculated distributions is striking and even the details at the single pore scale seem to be correctly replicated. From this example we can see how a dynamic SXR- μ CT experiment opens new opportunities to both develop *and validate* models. The resulting software tool provides a validated approach to predicting the distribution of scCO₂ during drainage in porous media, requiring only a dry XR- μ CT dataset of a reservoir sandstone.

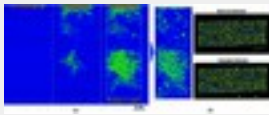


Figure 6

(a) Sequence of projections showing the invasion process (from the top) of scCO₂ displacing the brine. (b) The equivalent projection calculated from the model (left). Selected subvolumes displaying 3D details of the distribution of the fluids (cyan: brine; yellow: scCO₂) in both the measured and calculated datasets to show the accuracy of the model at the single pore scale.

2.4. Uniaxial stress: closing a fracture filled with proppant in a shale

The current technique of choice to exploit gas shales is hydraulic fracturing, where pressurized fluids are used to fracture the reservoir rock and proppant material is injected into the fractures to aid gas recovery by preventing their closure (Curtis, 2002). Understanding the mechanisms involved in the closure of fractures and the role of different proppants at the micro-scale could lead, for example, to improved proppant mixtures, but literature studies on this topic have usually been either theoretical (Phatak *et al.*, 2013) or empirical, generally tackling the problem at the field scale (Barree *et al.*, 2002). Gradual reductions in fracture productivity have been hypothesized to be caused by some mixture of proppant embedment, proppant redistribution, proppant fracturing, fines migration and near-fracture transport limitations. Little is known about the importance of these processes at the pore scale where observations are generally difficult.

A ~6 mm core of Mancos shale, with the lamination plane roughly horizontal, was mounted in the environmental cell (Fig. 1a) and glued to the two endcaps. The sample was fractured under tension along a lamination layer, simulating the fracturing process, and the fracture was filled with the proppant mixture (sand and guar gel). Then a load was progressively applied from the top piston to induce the closure of the fracture. Data were collected using 30 keV monochromatic X-rays, with an exposure time of 310 ms for each of the 1801 projections. Pixel size was 1.8 μ m and the sample-to-detector distance was ~12 cm. Fig. 7(a) displays a sequence of volume renderings of the

sample (with a vertical digital cut) during the loading process, showing the evolution of the sample during the closure of the fracture. It is clear from these images that, during compression, the quartz grains trigger the generation of new cracks, spalling the sample where the tips are in contact with the shale; additionally, the grains themselves are subject to a surprisingly early failure, an undesired behavior for practical applications where fines generated by proppant failure might occlude the fracture at downstream locations. The cell can record the pressure applied to the vertical piston, and a linear variable differential transducer can record the vertical displacement: in Fig. 7(b) we plot the load and vertical displacement during the experiment, with labels corresponding to the frame number of the images in Fig. 7(a). The plot displays the vertical stress and displacement *versus* time, following the experiment at the beamline.



Figure 7

(a) Volume rendering of the propped fractured Mancos shale sample during closure (vertical cut). (b) The corresponding uniaxial stress + vertical displacement *versus* time of the experiment at the various steps (see numbering).

We used a DIC approach (Eberl *et al.*, 2006) to quantify local strain variations in the sample over time, as shown in Fig. 8. The top panel shows one vertical digital slice of the sample at time frames #3 to #5, while the bottom panel shows the results of horizontal and vertical DIC analysis for images #3 and #4. In the vertical DIC, the top mobile core section is shown to be descending as expected, as highlighted by the color scale representing the displacement. A weaker vertical displacement feature, emanating upwards from the upper tip of the largest sand grain (see arrow in figure), is also visible. This is likely due to a stress accumulation in that part of the sample, generated by the sharp corner of the proppant grain. The horizontal DIC shows smaller displacements, and can detect the breakage of a chip from the sand grain, given its lateral movement. Again a localized strain feature is visible in the horizontal DIC map above the grain corner before failure. Fig. 8, panel #5 (top), shows the location of the shale failure close to the DIC observed micro-strain features at previous time points. This demonstrates the ability of DIC-based approaches to provide local strain information, which can also be predictive of later stage failure.

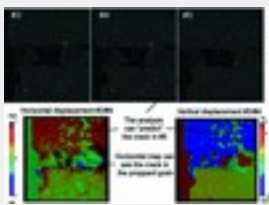


Figure 8

Digital image correlation (DIC) applied to a vertical section of the sample showing the role of a proppant sand grain in starting a crack. From this example it is also possible to see the potential of DIC as a predictive tool for the development of cracks.

From this dynamic SXR- μ CT experiment we have been able to observe and quantify some important mechanisms occurring at the micrometer scale which can potentially have an impact on the

development of new gas and oil shale exploitation strategies, *via*, for example, the development of more resistant and less fracture-inducing proppants.

2.5. Chemical dissolution: aqueous CO₂-induced limestone dissolution

Some reservoir rocks targeted for GCS chemically react with aqueous CO₂, which can, to an extent, be a desirable behavior when, for example, CO₂ reacts to form carbonates in a mineral trapping (Giammar *et al.*, 2005), or enhanced oil recovery (Blunt *et al.*, 1993) scenarios.

We designed an experiment to match the situation of a saturated CO₂ aqueous solution flowing in a low-pressure reservoir, simulating a very shallow aquifer, a possible context of a zone close to the injection well in proximity to the surface. We chose a sample of Bedford limestone (Indiana, USA), a complex biogenic limestone with significant recrystallization history and many convoluted microstructures mimicking the old fine structures of the foraminifera, bryozoa, *etc.* fragments comprising most of the rock sample.

The sample was cut as a $\sim 8.6 \times 7.7$ mm cylinder (fully imaged in the experiment) and jacketed with a heat-shrink sleeve including two stainless steel threaded-end couplings (Fig. 1d). An aqueous solution, pre-saturated with CO₂, was flowed through the sample (top to bottom) at a rate of 0.2 ml min⁻¹, with a fluid pressure of ~ 11 psi (76 kPa). A total of ten tomographic datasets were collected in 4 h increments under these conditions. Data were collected using filter-hardened white X-rays, with an exposure time of 80 ms for each of the 1441 projections. A pixel size of 4.44 μ m was utilized and the sample-to-detector distance was ~ 5 cm. A vertical cutout of the sample is visualized in the renderings in Fig. 9. The sequence shows that the dissolution starts close to the inlet (top of the sample) where small, isolated, features dissolve first, and that over time a preferential path of dissolution becomes more apparent (Fredd & Fogler, 1998; Maheshwari *et al.*, 2013) as the dissolution proceeds, similarly to the experiment of Menke *et al.* (2016).



Figure 9

Vertical cut of renderings showing the development of the Bedford limestone sample during dissolution. Each step corresponds to 4 h of reaction in a CO₂-saturated low-pressure aqueous solution.

With the evolution of the porosity in the sample, the entry pressure for a non-wetting fluid, such as scCO₂, would change significantly. Changes in entry pressure would make drainage processes easier, and the migration of the non-wetting fluid would be facilitated. Having a series of ten tomographic volumes available for data processing, we can apply the model we used in the Domengine sandstone example described in the example #3 of this article to calculate a capillary pressure curve for *each* volume of the series. This would simulate a scCO₂ drainage process under deeper reservoir conditions of a sample with evolving porosity by dissolution: a digital rock physics approach enabled by our measurement. The result of this operation becomes a capillary




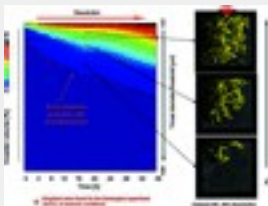
pressure 3D surface, instead of the experimental curves commonly measured in specific experiments, with a time *versus* throat diameter threshold *versus* invaded volume parametrization (plotted in Fig. 10 ). Since this plot only contains geometrical terms, it could be properly rescaled for different systems (e.g. scCO₂ drainage, mercury intrusion porosimetry, etc.) translating the throat size to capillary pressure. The dotted black line in the figure is the limit for scCO₂ under the reservoir conditions used in the high-pressure scCO₂ Domenegine experiment described above, showing that under those conditions the unreacted limestone sample would not have been invaded by the scCO₂ (at the right side, *i.e.* the unreacted sample, is below the entry pressure value) whereas after the evolution of the pore space due to the dissolution, up to 9% (at the end of the experiment) of the total volume could be invaded by scCO₂. The orange dotted line in Fig. 10  shows the evolution of the entry pressure, significantly decreasing with the increase in porosity. The 3D plot in the figure has been obtained by calculating ~1000 full volumes (~1.5 TB of data) of the invading fluid: a volume for each point in the capillary pressure surface. Three of these volumes (superimposed to a cutout volume rendering of the actual sample) are shown in Fig. 10  to visualize how the calculated invading fluid volume (rendered in yellow) looks in context.

Figure 10



Modeled capillary pressure plot (surface) showing the changes of the system with the reaction. The entry pressure changes markedly with the evolution of the pore space. Each point in the surface corresponds to a calculated volume with the invasion of the non-wetting fluid; three volumes, superimposed with a cut rendering of the real sample, are shown. On the *x* axis there is the dissolution extent, *i.e.* the increase in porosity due to the dissolution. The *y* axis corresponds to the throat diameter threshold used in the invasion model, which is inversely proportional to the capillary pressure




This last example highlights how SXR- μ CT is an extremely suitable technique to follow reactive systems in real time. The datasets generated, besides giving quantitative information about the evolving system, such as porosity increase *etc.*, are especially important from a modeling perspective and can also lead to information that is impossible to be measured *via* experimental techniques, such as the capillary-pressure surface shown. This also emphasizes again how the synergy of dynamic tomographic techniques and modeling is an approach that is rapidly growing in many research fields, with the specific case of digital rock physics in earth sciences.



3. Discussion and conclusions

We have presented a review of five different 4D SXR- μ CT experiments, performed at the 8.3.2 beamline at the ALS, related to climate change and fossil fuel topics to show their importance as a tool in the field of earth sciences. Recent developments in instrumentation allow these kinds of experiments; future improvements in the endstation design and environmental cells will likely




increase the popularity of such studies. Concerning 4D SXR imaging, there are a variety of different areas where advances are likely to occur as follows.

3.1. Storage ring and beamline optics

With the design of new lattices for storage rings, using new generation insertion devices, the brilliance and coherence of the X-ray beam will be significantly increased. The higher photon flux at the sample will allow faster data collection, clearly a key parameter in dynamic imaging experiments. The higher flux will also make less conventional tomographic techniques such as pencil beam X-ray diffraction tomography (XRD-CT) and micro-X-ray fluorescence tomography (μ XRF-CT) more appealing with faster data collection times available for time-resolved measurements in evolving systems; the first example of pencil beam dynamic XRD-CT imaging, following cement hydration, can be found by Voltolini *et al.* (2013 ) and clearly shows some of its current limitations. The higher spatial coherence of the X-ray beam will also push the development of techniques more related to diffractive imaging. Lattice upgrades moving towards this direction are planned in the few next years at several light sources, e.g. ALS (ALS-U; see Tarawneh *et al.*, 2014 ) and ESRF (Upgrade Phase II, 2015–2019; Revol *et al.*, 2014 )

The improvements on the detectors side also play a key role in increasing the data quality but especially the acquisition speed. The high intensity of the synchrotron X-rays, coupled with faster sensors, embedded memory and faster data transfer, now allows monitoring in 4D of very fast processes such as the development of gas in synthetic lava samples (Baker *et al.*, 2012 ) or Haines jumps during multiphase flow in a sandstone sample (Berg *et al.*, 2013 )







3.2. Sample environmental chambers






Sample environmental chambers are critical to the fourth dimension in dynamic SXR- μ CT experiments since they control the parameter (e.g. temperature) that induces changes in the sample. With the increase in data collection speed, the engineering of new environmental sample chambers becomes a crucial asset for beamlines and opens new challenges and opportunities for users. Both synchrotron imaging beamlines and conventional X-ray scanner vendors are exploring this path, with commercial environmental chambers becoming increasingly available worldwide. It is easy to foresee that in the future better chambers will be available to the users, with the two main paths being pursued being as follows. (i) More extreme conditions, for example in terms of P and T , such as improved Paris–Edinburgh cells (Bromley *et al.*, 2009 ; Álvarez-Murga *et al.*, 2011 ) or panoramic diamond anvil cells used for SXR diffraction (Mao *et al.*, 2001 ) optimized for SXR- μ CT. (ii) More parameters combined in the same chamber, for example the cell developed at the ALS shown in the present work, where combinations of tension, compression, controlled chemical environment (gas) and heating can be used in a single data collection run. In the field of earth sciences the ability to combine multiple parameters opens new opportunities for studies of complex

mechanisms, such as rock deformation studies under non-ambient conditions, with implications in rock mechanics in general, volcanology, structural geology or even planetary science.

3.3. Software





There are a number of new developments in this fast-evolving area.

(i) *Development of novel reconstruction algorithms and strategies.* As of today, the common procedure for a SXR- μ CT experiment is to apply a filtered backprojection algorithm to the (flat-field-corrected) projections collected over a 180° rotation in equal angular increments. Different algorithms for the volume reconstructions from projections have been developed in the past, but are still very rarely used with conventional SXR- μ CT, mainly because of their intensive CPU requirements. They are, however, often used with other tomographic techniques (electron tomography, positron emission tomography, XRD-CT, μ XRF-CT, etc.). Examples include the algebraic reconstruction technique (Gordon *et al.*, 1970 ) , the simultaneous algebraic reconstruction technique (Andersen & Kak, 1984 ) , the simultaneous iterative reconstruction technique (Gilbert, 1972 ) and maximum likelihood expectation maximization (Lange *et al.*, 1987 ) . New reconstruction techniques more oriented towards XR-CT allowing for faster and better quality results are currently being developed, and different concepts are applied, such as model-based iterative reconstruction procedures (Mohan *et al.*, 2014 ) , or procedures aimed at the super-resolution (Miao *et al.*, 2005 ) .

(ii) *Morphometric analysis of the data.* The quantification of the microstructural features in XR-CT datasets requires specific software for 3D datasets manipulation and analysis. Different commercial packages are available (e.g. *Avizo*®; Visualization Science Group, Burlington, MA, USA), but specific packages are also being developed directly at SXR imaging beamlines [e.g. *iMorph*, developed at the ESRF (Brun & Camille, 2009 ) ; *Pore3D* at SYRMEP at the Elettra synchrotron (Brun *et al.*, 2010 )]. Extremely powerful generic image processing packages also exist, such as the *DIPimage* and *DIPlib* libraries for *Matlab*® (Hendriks *et al.*, 1999 ) or *Fiji* (Schindelin *et al.*, 2012 ) . The need for more tomography-specific image processing tools is growing, and new approaches based on machine-learning concepts such as computer vision are starting to be developed (Chauhan *et al.*, 2016 ) .

(iii) *Modeling.* Often the modeler has no realistic starting point, or results, to validate a model. This often leads to oversimplifications which could lead to incorrect results. A clear example of the issues caused by oversimplification in describing microstructures in models has also been shown in our permafrost experiment. 4D SXR- μ CT is the most useful when used both to provide a starting point for the model and to act as a validation for the model itself, as we have clearly shown in the example of the scCO₂ drainage in a sandstone, where the baseline dataset was used as a starting point for the model and the real data of the scCO₂ used to check the similarity of the calculated and

measured distributions of the fluids. In this scenario, synergistic collaboration of X-ray imaging experimentalists and modelers are becoming a fundamental asset for research groups to build generalized predictive tools.

All of the three points above can require some substantial computational power. The increasing availability of facilities able to perform highly demanding computational processes will take full advantage of the software improvements. Many SXR- μ CT beamlines are routinely using off-site super-computing facilities for a close-to-real-time 3D reconstruction of the datasets collected at the beamline, with the current preferred method being based on *gridrec* (Dowd *et al.*, 1999 ) and implemented at different X-ray tomography synchrotron beamlines (e.g. Marone *et al.*, 2010 ; Gürsoy *et al.*, 2014 ; Parkinson *et al.*, 2016 ). Of course, scientists carrying out data analysis and modeling are also starting to take advantage of large computational facilities, as the datasets are becoming larger and larger, and the models increasingly complex as well.

As demonstrated through a survey of examples from just a single beamline equipped for dynamic X-ray imaging, the new opportunities opened by 4D SXR- μ CT are remarkable. SXR- μ CT in earth sciences will grow in importance, with improvements at synchrotron light source facilities, new data analysis software development and the collaboration between experimentalists and modelers; we hope this combination will foster the development of solutions for existing challenges in the geosciences, including climate change mitigation and more efficient energy production.

Footnotes

[‡]Now at Nikon Research Corporation of America, Belmont, USA.

Acknowledgements

Benjamin Delattre at the Lawrence Berkeley National Laboratory is acknowledged for allowing us the use of the cooling stage for the freezing experiment.

Funding information

The following funding is acknowledged: Center for Nanoscale Control of Geologic CO₂ (NCGC – EFRC) of the US Department of Energy, Office of Science, Office of Basic Energy Sciences, Energy Frontier Research Centers program (award No. DE-AC02-05CH11231); Next Generation Ecosystem Experiment (NGEE-Arctic) project, sponsored by the Office of Biological and Environmental Research in the DOE Office of Science (award No. DEAC0205CH11231); Stanford Total Enhanced Modeling of Source Rock (STEMS); US DOE, Office of Fossil Energy, Office of Natural Gas and Petroleum Technology, through the National Energy Technology Laboratory (award No. DE-AC02-05CH11231, with support from the project ESD14089); The Advanced Light Source is supported by the Director, Office of Science, Office of Basic Energy Sciences, of the US Department of Energy (award No. DE-AC02-05CH11231).

References

- ↑ Álvarez-Murga, M., Bleuet, P., Marques, L., Lepoittevin, C., Boudet, N., Gabarino, G., Mezouar, M. & Hodeau, J.-L. (2011). *J. Appl. Cryst.* **44**, 163–171. [Web of Science](#) [CrossRef](#) [IUCr Journals](#) [Google Scholar](#)
- ↑ Andrew, M., Bijeljic, B. & Blunt, M. J. (2013). *Geophys. Res. Lett.* **40**, 3915–3918. [Web of Science](#) [CrossRef](#) [CAS](#) [Google Scholar](#)
- ↑ Andersen, A. H. & Kak, A. C. (1984). *Ultrasonic Imaging*, **6**, 81–94. [CrossRef](#) [CAS](#) [PubMed](#) [Google Scholar](#)
- ↑ Arganda-Carreras, I., Sorzano, C. O., Kybic, J. & Ortiz-de-Solorzano, C. (2008). *Second ImageJ User and Developer Conference*, 7–8 November 2008, Luxembourg. [Google Scholar](#)
- ↑ Armstrong, R. T., Georgiadis, A., Ott, H., Klemin, D. & Berg, S. (2014). *Geophys. Res. Lett.* **41**, 55–60. [Web of Science](#) [CrossRef](#) [Google Scholar](#)
- ↑ Baker, D. R., Brun, F., O'Shaughnessy, C., Mancini, L., Fife, J. L. & Rivers, M. (2012). *Nat. Commun.* **3**, 1135. [Web of Science](#) [CrossRef](#) [PubMed](#) [Google Scholar](#)
- ↑ Bale, H. A., Haboub, A., MacDowell, A. A., Nasiatka, J. R., Parkinson, D. Y., Cox, B. N., Marshall, D. B. & Ritchie, R. O. (2013). *Nat. Mater.* **12**, 40–46. [CrossRef](#) [CAS](#) [PubMed](#) [Google Scholar](#)
- ↑ Barree, R. D., Fisher, M. K. & Woodroof, R. A. (2002). *SPE Annual Technical Conference and Exhibition*. Society of Petroleum Engineers. [Google Scholar](#)
- ↑ Berg, S., Ott, H., Klapp, S. A., Schwing, A., Neiteler, R., Brussee, N., Makurat, A., Leu, L., Enzmann, F., Schwarz, J. O., Kersten, M., Irvine, S. & Stampanoni, M. (2013). *Proc. Natl Acad. Sci.* **110**, 3755–3759. [Web of Science](#) [CrossRef](#) [CAS](#) [PubMed](#) [Google Scholar](#)
- ↑ Besson, J. M., Nelmes, R. J., Hamel, G., Loveday, J. S., Weill, G. & Hull, S. (1992). *Physica B*, **180–181**, 907–910. [CrossRef](#) [CAS](#) [Web of Science](#) [Google Scholar](#)
- ↑ Blunt, M., Fayers, F. J. & Orr, F. M. (1993). *Energy Convers. Manage.* **34**, 1197–1204. [CrossRef](#) [CAS](#) [Web of Science](#) [Google Scholar](#)
- ↑ Bray, H. J., Redfern, S. A. & Clark, S. M. (1998). *Min. Mag.* **62**, 647–656. [Web of Science](#) [CrossRef](#) [CAS](#) [Google Scholar](#)
- ↑ Bromiley, G. D., Redfern, S. A., Le Godec, Y., Hamel, G. & Klotz, S. (2009). *High. Press. Res.* **29**, 306–316. [Web of Science](#) [CrossRef](#) [CAS](#) [Google Scholar](#)
- ↑ Brun, E. & Camille, M. (2009). PhD dissertation, Aix Marseille 1. France. [Google Scholar](#)
- ↑ Brun, F., Mancini, L., Kasae, P., Favretto, S., Dreossi, D. & Tromba, G. (2010). *Nucl. Instrum. Methods Phys. Res. A*, **615**, 326–332. [Web of Science](#) [CrossRef](#) [CAS](#) [Google Scholar](#)
- ↑ Chauhan, S., Rühaak, W., Anbergen, H., Kabdenov, A., Freise, M., Wille, T. & Sass, I. (2016). *Solid Earth*, **7**, 1125–1139. [Web of Science](#) [CrossRef](#) [Google Scholar](#)
- ↑ Cnudde, V. & Boone, M. N. (2013). *Earth Sci. Rev.* **123**, 1–17. [Web of Science](#) [CrossRef](#) [Google Scholar](#)
- ↑ Curtis, J. B. (2002). *AAPG Bull.* **86**, 1921–1938. [CAS](#) [Google Scholar](#)
- ↑ Di Michiel, M., Merino, J. M., Fernandez-Carreiras, D., Buslaps, T., Honkimäki, V., Falus, P., Martins, T. & Svensson, O. (2005). *Rev. Sci. Instrum.* **76**, 043702. [Web of Science](#) [CrossRef](#) [Google Scholar](#)
- ↑ Dou, S., Nakagawa, S., Dreger, D. & Ajo-Franklin, J. (2016). *Geophysics*, **81**, WA233–

WA245. [Web of Science](#) [CrossRef](#) [Google Scholar](#)



Dou, S., Nakagawa, S., Dreger, D. & Ajo-Franklin, J. (2017). *Geophysics*, **82**, EN33–

EN50. [Web of Science](#) [CrossRef](#) [Google Scholar](#)



Dougherty, R. & Kunzelmann, K. H. (2007). *Microsc. Microanal.* **13**, 1678. [CrossRef](#) [Google Scholar](#)



Dowd, B. A., Campbell, G. H., Marr, R. B., Nagarkar, V. V., Tipnis, S. V., Axe, L. & Siddons, D. P. (1999). *Proc. SPIE*, **3772**, 224–236. [CrossRef](#) [Google Scholar](#)



Dunsmuir, J. H., Bennett, S., Fareria, L., Mingino, A. & Sansone, M. (2006). *Powder Diffr.* **21**, 125–

131. [Web of Science](#) [CrossRef](#) [CAS](#) [Google Scholar](#)



Eberl, C., Thompson, R., Gianola, D., Sharpe, W. Jr & Hemker, K. (2006). *Digital image correlation and tracking*. MatLabCentral, Mathworks file exchange server, FileID 12413. [Google Scholar](#)



Ferrage, E., Kirk, C. A., Cressey, G. & Cuadros, J. (2007). *Am. Mineral.* **92**, 994–

1006. [Web of Science](#) [CrossRef](#) [CAS](#) [Google Scholar](#)



Fredd, C. N. & Fogler, H. S. (1998). *AIChE J.* **44**, 1933–1949. [Web of Science](#) [CrossRef](#) [CAS](#) [Google Scholar](#)



Fusseis, F., Steeb, H., Xiao, X., Zhu, W., Butler, I. B., Elphick, S. & Mäder, U. (2014b). *J. Synchrotron Rad.* **21**, 251–253. [Web of Science](#) [CrossRef](#) [CAS](#) [IUCr Journals](#) [Google Scholar](#)



Fusseis, F., Xiao, X., Schrank, C. & De Carlo, F. (2014a). *J. Struct. Geol.* **65**, 1–

16. [Web of Science](#) [CrossRef](#) [Google Scholar](#)



Giammar, D. E., Bruant, R. G. & Peters, C. A. (2005). *Chem. Geol.* **217**, 257–

276. [Web of Science](#) [CrossRef](#) [CAS](#) [Google Scholar](#)



Gilbert, P. (1972). *J. Theor. Biol.* **36**, 105–117. [CrossRef](#) [CAS](#) [PubMed](#) [Web of Science](#) [Google Scholar](#)



Gordon, R., Bender, R. & Herman, G. T. (1970). *J. Theor. Biol.* **29**, 471–

481. [CrossRef](#) [CAS](#) [PubMed](#) [Web of Science](#) [Google Scholar](#)



Gualda, G. A., Baker, D. R. & Polacci, M. (2010). *Geosphere* **6**, 468–

469. [Web of Science](#) [CrossRef](#) [Google Scholar](#)



Gürsoy, D., De Carlo, F., Xiao, X. & Jacobsen, C. (2014). *J. Synchrotron Rad.* **21**, 1188–

1193. [Web of Science](#) [CrossRef](#) [IUCr Journals](#) [Google Scholar](#)



Hendriks, C. L., Van Vliet, L. J., Rieger, B., van Kempen, G. M. P. & van Ginkel, M. (1999). *DIPimage: a scientific image processing toolbox for MATLAB*, Delft University of Technology, Delft, The Netherlands. [Google Scholar](#)



Herzog, H. J. (2001). *Environ. Sci. Technol.* **35**, 148A–

153A. [Web of Science](#) [CrossRef](#) [PubMed](#) [CAS](#) [Google Scholar](#)



Hu, Q., Qian, G. & Nowinski, W. L. (2005). *Comput. Vis. Image Underst.* **99**, 414–

434. [Web of Science](#) [CrossRef](#) [Google Scholar](#)



Iglauer, S., Paluszny, A. & Blunt, M. J. (2013). *Fuel*, **103**, 905–

914. [Web of Science](#) [CrossRef](#) [CAS](#) [Google Scholar](#)



Kerkar, P. B., Horvat, K., Jones, K. W. & Mahajan, D. (2014). *Geochem. Geophys. Geosyst.* **15**, 4759–

4768. [Web of Science](#) [CrossRef](#) [CAS](#) [Google Scholar](#)

- ↑ Ketcham, R. A. (2005). *J. Struct. Geol.* **27**, 1217–1228. [Web of Science](#) [CrossRef](#) [Google Scholar](#)
- ↑ Koven, C. D., Ringeval, B., Friedlingstein, P., Ciais, P., Cadule, P., Khvorostyanov, D., Krinner, G. & Tarnocai, C. (2011). *Proc. Natl Acad. Sci.* **108**, 14769–14774. [Web of Science](#) [CrossRef](#) [CAS](#) [PubMed](#) [Google Scholar](#)
- ↑ Landry, C. J., Karpyn, Z. T. & Ayala, O. (2014). *Transport Porous Med.* **103**, 449–468. [Web of Science](#) [CrossRef](#) [CAS](#) [Google Scholar](#)
- ↑ Lange, K., Bahn, M. & Little, R. (1987). *IEEE Trans. Med. Imaging*, **6**, 106–114. [CrossRef](#) [PubMed](#) [CAS](#) [Web of Science](#) [Google Scholar](#)
- ↑ Le Godec, Y., Hamel, G., Martinez-Garcia, D., Hammouda, T., Solozhenko, V. L. & Klotz, S. (2005). *High. Press. Res.* **25**, 243–253. [Web of Science](#) [CrossRef](#) [CAS](#) [Google Scholar](#)
- ↑ MacDowell, A. A., Parkinson, D. Y., Haboub, A., Schaible, E., Nasiatka, J. R., Yee, C. A., Jameson, J. R., Ajo-Franklin, J. B., Brodersen, C. R. & McElrone, A. J. (2012). *Proc. SPIE*, **8506**, 850618. [CrossRef](#) [Google Scholar](#)
- ↑ Maheshwari, P., Ratnakar, R. R., Kalia, N. & Balakotaiah, V. (2013). *Chem. Eng. Sci.* **90**, 258–274. [Web of Science](#) [CrossRef](#) [CAS](#) [Google Scholar](#)
- ↑ Mao, H. K., Kao, C. & Hemley, R. J. (2001). *J. Phys. Condens. Matter*, **13**, 7847–7858. [Web of Science](#) [CrossRef](#) [CAS](#) [Google Scholar](#)
- ↑ Marone, F., Münch, B. & Stampanoni, M. (2010). *Proc. SPIE*, **7804**, 780410. [CrossRef](#) [Google Scholar](#)
- ↑ Menke, H. P., Andrew, M. G., Blunt, M. J. & Bijeljic, B. (2016). *Chem. Geol.* **428**, 15–26. [Web of Science](#) [CrossRef](#) [CAS](#) [Google Scholar](#)
- ↑ Metz, B., Davidson, O., De Coninck, H., Loos, M. & Meyer, L. (2005). *Carbon dioxide capture and storage*. <http://digital.library.unt.edu/Ark:/67531/metadc12051/>. [Google Scholar](#)
- ↑ Miao, J., Förster, F. & Levi, O. (2005). *Phys. Rev. B*, **72**, 052103. [Web of Science](#) [CrossRef](#) [Google Scholar](#)
- ↑ Mohan, K. A., Venkatakrishnan, S. V., Drummy, L. F., Simmons, J., Parkinson, D. Y., & Bouman, C. A. (2014). *2014 IEEE International Conference on Acoustics, Speech and Signal Processing (ICASSP)*, pp. 6909–6913. [Google Scholar](#)
- ↑ Panahi, H., Kobchenko, M., Renard, F., Mazzini, A., Scheibert, J., Dysthe, D. K., Jamtveit, B., Malthe-Sørensen, A. & Meakin, P. (2014). *arXiv:1401.2448*. [Google Scholar](#)
- ↑ Parkinson, D. Y., Beattie, K., Chen, X., Correa, J., Dart, E., Daurer, B. J., Deslippe, J. R., Hexemer, A., Krishnan, H., MacDowell, A. A., Maia, F. R. N. C., Marchesini, S., Padmore, H. A., Patton, S. J., Perciano, T., Sethian, J. A., Shapiro, D., Stromsness, R., Tamura, N., Tierney, B. L., Tull, C. E. & Ushizima, D. (2016). *AIP Conf. Proc.* **1741**, 050001. [Google Scholar](#)
- ↑ Phatak, A., Kresse, O., Neuvonen, O. V., Abad, C., Cohen, C. E., Lafitte, V., Abivin, P., Weng, X. & England, K. W. (2013). *SPE Hydraulic Fracturing Technology Conference*, 4–6 February 2013, The Woodlands, Texas, USA. Society of Petroleum Engineers. [Google Scholar](#)
- ↑ Renard, F., Cordonnier, B., Dysthe, D. K., Boller, E., Tafforeau, P. & Rack, A. (2016). *J. Synchrotron Rad.* **23**, 1030–1034. [Web of Science](#) [CrossRef](#) [CAS](#) [IUCr Journals](#) [Google Scholar](#)
- ↑ Revol, J. L., Berkvens, P., Biasci, J. C., Bouteille, J. F., Carmignani, N., Chavanne, J., Ewald, F., Farvacque, L.,

- Goirand, L., Hahn, M. & Hardy, L. (2014). *Proceedings of IPAC2014*, Dresden, Germany, pp. 209–211. [Google Scholar](#)
- ↑ Rivers, M. L., Sutton, S. R. & Eng, P. (1999). *Proc. SPIE*, **3772**, 78–86. [CrossRef](#) [Google Scholar](#)
- ↑ Rivers, M. L. & Wang, Y. (2006). *Proc. SPIE*, **6318**, 63180J. [CrossRef](#) [Google Scholar](#)
- ↑ Schindelin, J., Arganda-Carreras, I., Frise, E., Kaynig, V., Longair, M., Pietzsch, T., Preibisch, S., Rueden, C., Saalfeld, S., Schmid, B., Tinevez, J. Y., White, D. J., Hartenstein, V., Eliceiri, K., Tomancak, P. & Cardona, A. (2012). *Nat. Methods*, **9**, 676–682. [Web of Science](#) [CrossRef](#) [CASPubMed](#) [Google Scholar](#)
- ↑ Silin, D., Tomutsa, L., Benson, S. M. & Patzek, T. W. (2011). *Transport Porous Media*, **86**, 495–515. [Web of Science](#) [CrossRef](#) [CAS](#) [Google Scholar](#)
- ↑ Sutton, S. J., Ethridge, F. G., Almon, W. R., Dawson, W. C. & Edwards, K. K. (2004). *AAPG Bull.* **88**, 1185–1206. [Web of Science](#) [CrossRef](#) [Google Scholar](#)
- ↑ Tarawneh, H., Steier, C., Falcone, R., Robin, D., Nishimura, H., Sun, C. & Wan, W. (2014). *J. Phys. Conf. Ser.* **493**, 012020. [CrossRef](#) [Google Scholar](#)
- ↑ Tiwari, P., Deo, M., Lin, C. L. & Miller, J. D. (2013). *Fuel*, **107**, 547–554. [Web of Science](#) [CrossRef](#) [CAS](#) [Google Scholar](#)
- ↑ Voltolini, M., Dalconi, M. C., Artioli, G., Parisatto, M., Valentini, L., Russo, V., Bonnin, A. & Tucoulou, R. (2013). *J. Appl. Cryst.* **46**, 142–152. [Web of Science](#) [CrossRef](#) [CAS](#) [IUCr Journals](#) [Google Scholar](#)
- ↑ Voltolini, M., Wenk, H. R., Mondol, N. H., Bjørlykke, K. & Jahren, J. (2008). *Geophysics*, **74**, D13–D23. [Web of Science](#) [CrossRef](#) [Google Scholar](#)
- ↑ Voltolini, M., Zandomenighi, D., Mancini, L. & Polacci, M. (2011). *J. Volcanol. Geotherm. Res.* **202**, 83–95. [Web of Science](#) [CrossRef](#) [CAS](#) [Google Scholar](#)
- ↑ Voltolini, M., Kwon, T.-K. & Ajo-Franklin, J. B. (2017). *Intl J. Greenhouse Gas Control*. In the press. [Google Scholar](#)
- ↑ Youssef, S., Rosenberg, E., Deschamps, H., Oughanem, R., Maire, E., & Mokso, R. (2014). *Proceedings of the Symposium of the Society of Core Analysts*, Montpellier, France, pp. 11–18. [Google Scholar](#)
- ↑ Yu, T., Wang, Y. & Rivers, M. L. (2016). *Prog. Earth Planet. Sci.* **3**, 1–13. [Web of Science](#) [CrossRef](#) [Google Scholar](#)
- ↑ Zhou, M., Lu, D., Dunsmuir, J. & Thomann, H. (2000). *Phys. Chem. Earth A*, **25**, 169–174. [Web of Science](#) [CrossRef](#) [Google Scholar](#)